Alumina doped Fe$_2$O$_3$ foams by freeze-casting for redox cycling applications

P.J. Lloreda-Jurado [a,b], Krishnakumar Balu [a], Jesús Hernández-Saz [a], E. Chicardi [a], Begoña Ferrari [b], R. Sepúlveda [a,*]

[a] Departamento de Ingeniería y Ciencia de los Materiales y del Transporte, E.T.S. de Ingenieros, Universidad de Sevilla, Avda. Camino de los Descubrimientos s/n., 41092 Sevilla, Spain
[b] Instituto de Cerámica y Vidrio (ICV), Madrid, Spain

ARTICLE INFO

ABSTRACT

Hydrogen is the next energy vector for a decarbonization society but industrial production is still methane-based. The Steam Iron Process (SIP) could provide a carbon-free production and safety storage option. Here, we show that a Fe$_2$O$_3$-3 wt% of Al$_2$O$_3$ foams created by freeze-casting withstand 10 redox cycles at different temperatures with no reduction in performance or pore shrinking. The use of stearic acid as a dispersant agent/binder produces the porous structure enhancement of the foam and promotes the early reduction of the hematite phase during foam sintering. The Al$_2$O$_3$ incorporation was detected as a solid solution in the Fe$_2$O$_3$ phase at the particle surface. This result is relevant as correlated the positive values of the zeta potential observed. Freeze-casted foams could improve long-term redox performances combining a unique tailored interconnected pore structure with a specific chemical composition.

1. Introduction

Over recent years, the need for a clean and renewable energy source is undeniable. The concentration of greenhouse gases from the overuse of fossil fuels is causing a global emergency [1]. Hydrogen is an energy vector that could counterbalance this harmful effect as no CO$_2$ is emitted during its consumption. However, large-scale hydrogen production is still methane-based [2]. A green and cost-effective method for hydrogen production and storage must involve the use of renewable resources (e.g. biomass) [3] with pre-existing technologies such as the Chemical Looping Hydrogen (CLH) [4] or Steam-Iron Process (SIP) [5,6]. The SIP is a two-step process, where an iron oxide (oxygen carrier) is exposed to a reducing gas stream, such as ethanol [7,8] or bioethanol, to turn it into metal iron, then a steam flow re-oxidizes the metal to Fe$_3$O$_4$ and produces pure hydrogen by splitting the water molecule, this process is repeated numerously until the iron oxide loses their redox capability. The use of bioethanol instead of must common methanol gas to produce hydrogen, reduces the operation temperatures and allows the revalorization of such renewable source [9,10].

Fe$_2$O$_3$ (hematite) is an abundant and inexpensive raw material with attractive oxygen carrier capability due to its redox properties [11–13].

However, the redox performance is deeply affected by the deactivation phenomena due to the sintering process after numerous redox cycles at high temperature. To prevent the deactivation, hematite has been doped with CeO$_2$ [6], La$_2$O$_3$ [14], CaO$_2$ [15,16], or Al$_2$O$_3$ [17]. Al$_2$O$_3$ additions are known to improve the cycle stability of Fe$_2$O$_3$ [11] and stabilize the amount of H$_2$ generated during continuous operation [18], it also increases the mechanical properties at higher temperatures due to its higher Tammann temperature [19]. Several methods to incorporate the Al$_2$O$_3$ into iron oxide particles have been studied, such as the mechanical mixing [20], impregnation [21], or co-precipitation [22]. Furthermore, Al$_2$O$_3$ as an additive shows limited solubility into the iron oxides structures and neglected solubility in Fe. During reduction, Al$_2$O$_3$ phase is consolidated and could form FeAl$_2$O$_4$ (hercynite) at the oxidation step which reduces the redox performance of the oxygen carrier [23]. An option to counterbalance this effect could be to limit the conversion of the iron oxides to full metal [17].

A new approach has been recently proposed, to replace the use of powder in the fluidized-bed systems by structural porous materials as oxygen carriers [24–26]. Freeze-casting (FC) is a manufacturing technique devoted to produce structural porous materials with different pore sizes and morphologies [27,28]. But also, it is a cost-effective near net
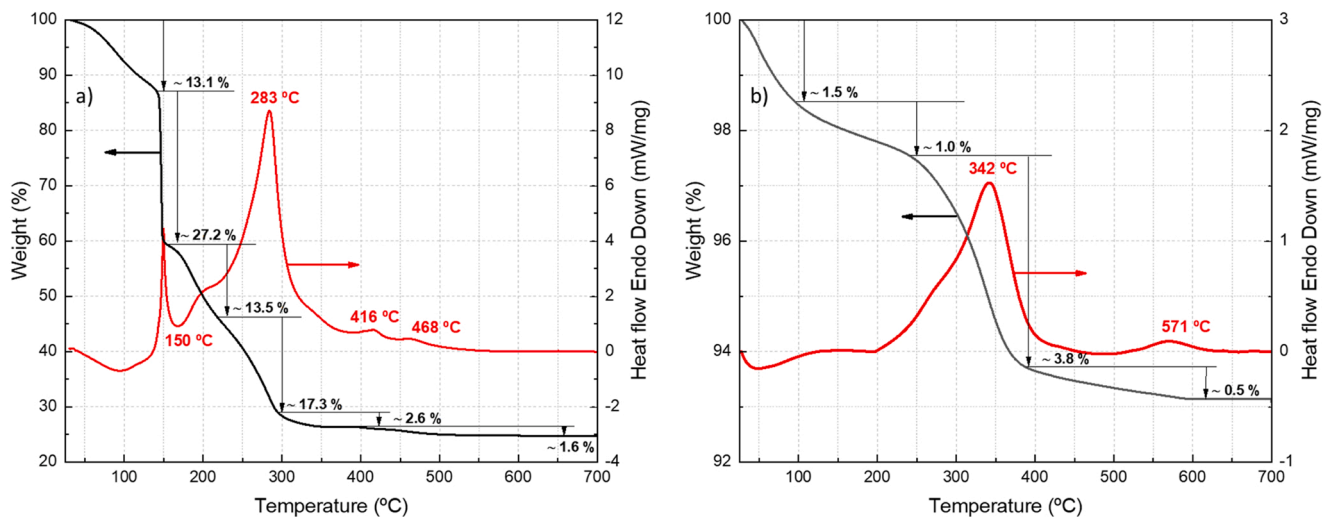

Fig. 1. TG (black lines) and DSC (red lines) curves of synthesized powder at different initial conditions: at gel form (a) and dried at 110 °C overnight (b). (For interpretation of the references to color in this figure legend, the reader is referred to the web version of this article.)
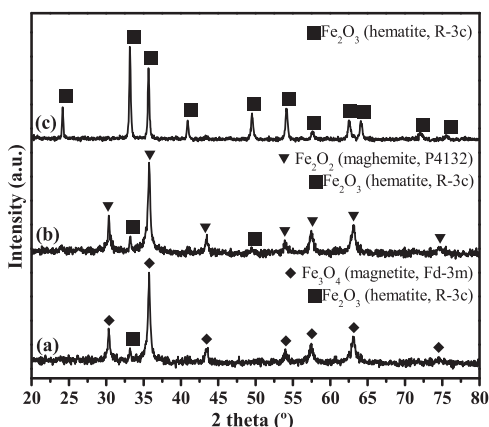

Fig. 2. XRD patterns of the synthesized powder (gel form) calcined at different temperatures: 170 °C (a), 350 °C (b) both for 2 h and 620 °C (c) for 6 h.

shaping (NNS) technology allowing foams fabrication in multiple sizes and shapes. However, pure Fe-foams manufactured by FC using water [29] and camphene-based [30,31] hematite slurries have shown a

significant modification of the pore structure after being subjected to several redox cycles. Authors have found a continuous reduction in the pore size due to the sintering of the Fe cell walls, which is especially critical when pores were under 30 μm in diameter [24]. Thus, the combination of an improved chemical formulation with the use of a highly interconnected pore structure with a high surface area could enhance the redox performance.

In this research, we have successfully manufactured Al_2O_3 doped Fe_2O_3 foams with an average pore size over 120 μm in diameter. The influences of the processing variables and the redox performance at different temperatures were studied. Redox cycles were conducted with a partial reduction step with hydrogen and an oxygen oxidation step to test the evolution of the pore structure with full reconversion to Fe_2O_3.

2. Experimental procedure

2.1. Powder synthesis

Doped Fe_2O_3 powders with 3 wt% of Al_2O_3 (named as Fe3Al) was synthesized using the citrate method previously described by Lorente et al. [32]. Briefly, 2 M aqueous solutions of selected metal nitrates (Fe $(NO_3)_3.9H_2O$ (98+% purity) and $Al(NO_3)_3.9H_2O$ (98% purity) with citric acid (99 +% purity) were mixed and stirred at 80 °C until a gel is
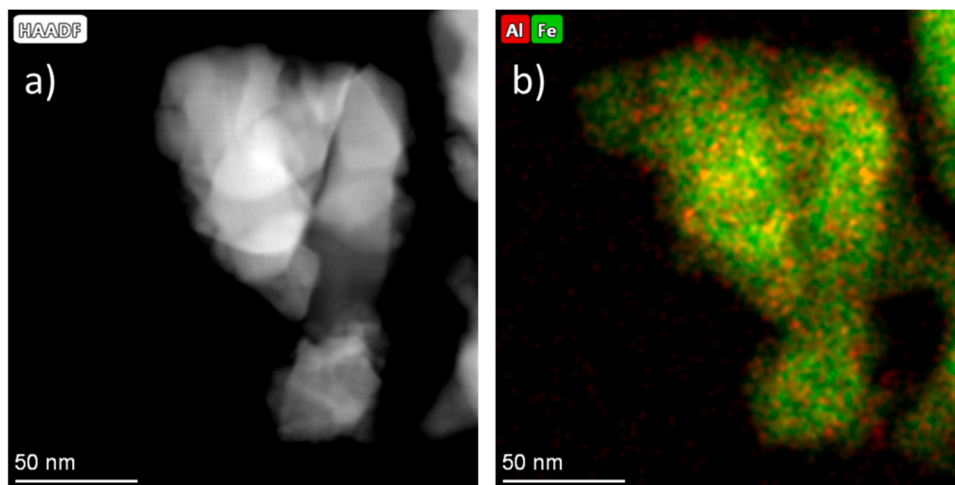

Fig. 3. High-Angle Annular Dark-Field (HAADF) image (a) and element distribution of Fe and Al by EDX analysis (b) of the Fe3Al calcined powder.
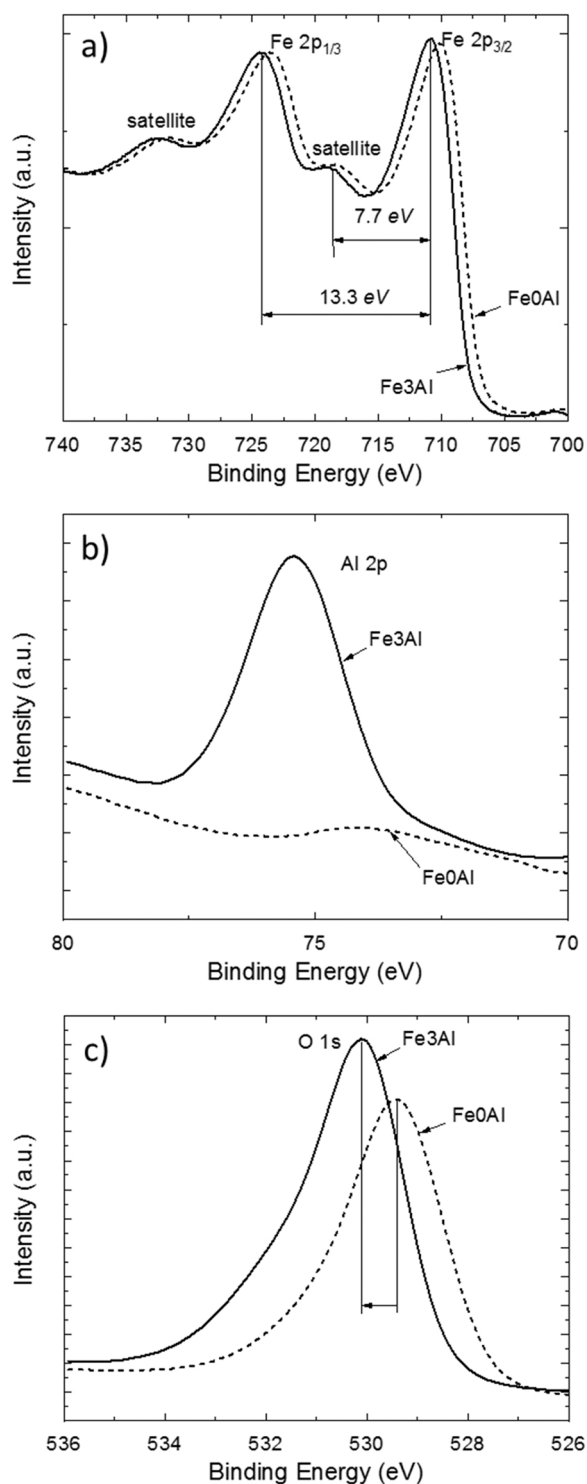
Fig. 4. High-resolution XPS spectra of Fe 2p (a), Al 2p (b), and O 1 s (c) of the Fe3Al and Fe0Al calcined powder after.

obtained. The molar ratio of citric acid to metal nitrates was set to 1 in the solution. The gels were dried overnight at 110 °C and calcined at 620 °C during 8 h. The synthesized powders were finally ball-milled for 24 h to reduce the particle size. All reactive agents were procured from Alfa Aesar™.

2.2. Foam manufacturing

Camphene (95% purity, Sigma Aldrich, Spain) slurries with 10 vol% of Fe3Al powder loading were produced by ball milling at 60 °C for 24 h using 1, 2, or 3 wt% of stearic acid –SA– (98% purity, Sigma Aldrich, Spain) related to the powder load, as dispersant agent. The SA was added and mixed with the camphene for 30 min prior the powder was incorporated.

After the ball milling, camphene suspensions were poured into a copper base with PFTE walls mould of 30 mm in diameter by 15 mm in height preheated at 60 °C placed inside an incubator. Directional solidification was promoted by running water at 42.5 °C through the mould base and gradually reducing the incubator temperature at 0.2 $°C·min^{-1}$ until the complete sample solidification. Once demoulding, samples were subjected to a 3-day camphene sublimation process at ambient conditions under forced airflow, to later being heat-treated in air at 600 °C for 2 h for organic-specimen burn-out and 1100 °C for 2 h for particle sintering. To avoid crack formation during sintering, heating and cooling rates were set at 1 $°C·min^{-1}$ and 5 °C·min-1, respectively. Foam manufacturing procedure was based on a previous study [33]. Finally, sintered Fe3Al foams samples of approximately 12 mm in height and 24 mm in diameter were manufactured.

2.3. Powder and foam characterization

Synthesized powders were characterized by Differential Scanning Calorimetric (DSC) and Thermal Gravimetric (TG) analysis using a Q20 calorimetry unit (TA Instruments, USA) in air to determine the optimal calcination temperature. The crystallographic phase and oxidation state were determined after calcination with XRD (X-Ray Diffraction; D8 Advance A25, Bruker) and XPS (X-ray Photoelectron Spectroscopy; Phoibos 150 MCD, SPECS) analysis, respectively. The particle morphology, size, and Al distribution were estimated by Transmission Electron Microscopy (TEM) using a TALOS F200S (FEI, USA) microscope.

To establish an optimal dispersant content in camphene media, calcined powders were suspended in EtOH (ethanol) with concentration of $0.1g·L^{-1}$, since camphene evaporation could disturb the measurement made using the Zetasizer Nano ZS equipment (Malvern Panalytical, UK). The pH was modified by adding drops of HNO_3 or Tetramethylammonium hydroxide (HTMA) to reach acid or basic values, respectively before power addition. Two pH fixed slurries (pH 6 and 9) were prepared with different content of SA (0–3 wt%). The particle size was also measured. After slurry preparation with camphene, a Tensor II spectrometer (Bruker. UK) was used to acquire the FTIR spectra in transmission mode on samples with different content of SA. About 1.5 mg of the green sample (after camphene sublimation) were diluted with KBr powder (1:100 ratio) to form thin pellets using uniaxial compression. The acquired spectra were collected with a resolution of 8 $scan·cm^{-1}$. Pore size distributions were characterized for powders processed with different amounts of SA, by Mercury Intrusion Porosimetry (MIP) using a Micromeritics AutoPore IV 9510 (USA), and by the N_2 adsorption/desorption isotherms and BET specific surface area with an Accelerated Surface Area & Porosimetry (ASAP) system (Micromeritics ASAP 2020 (USA).

The sintered Fe3Al foams were characterized by Scanning Electron Microscopy (SEM) performed on a TENEO microscope (FEI, USA) and an Optical Microscopy (OM) using a Nikon microscope MA100N across the entire heights to determine the pore morphology. The pore size and cell wall width were estimated by Image Analysis (IA) using the nonredundant maximum-sphere-fitted algorithm [34] of the ImageJ software over the OM images. To estimate the average pore diameter at different sample height, 6 OM images covering a total area of 20 mm^2 were used. Total porosity (%) of the sintered foam was determined throughout Archimedes' method by soaking the samples into boiling water for 5 h following a 24 h immersion in hot water.

A TG analysis, using a Discovery (TA Instrument, USA) analyser, was performed to evaluate the isothermal redox performance on subsamples of the sintered Fe3Al foams with 3 wt% of SA. Subsamples of 3x3x3 mm
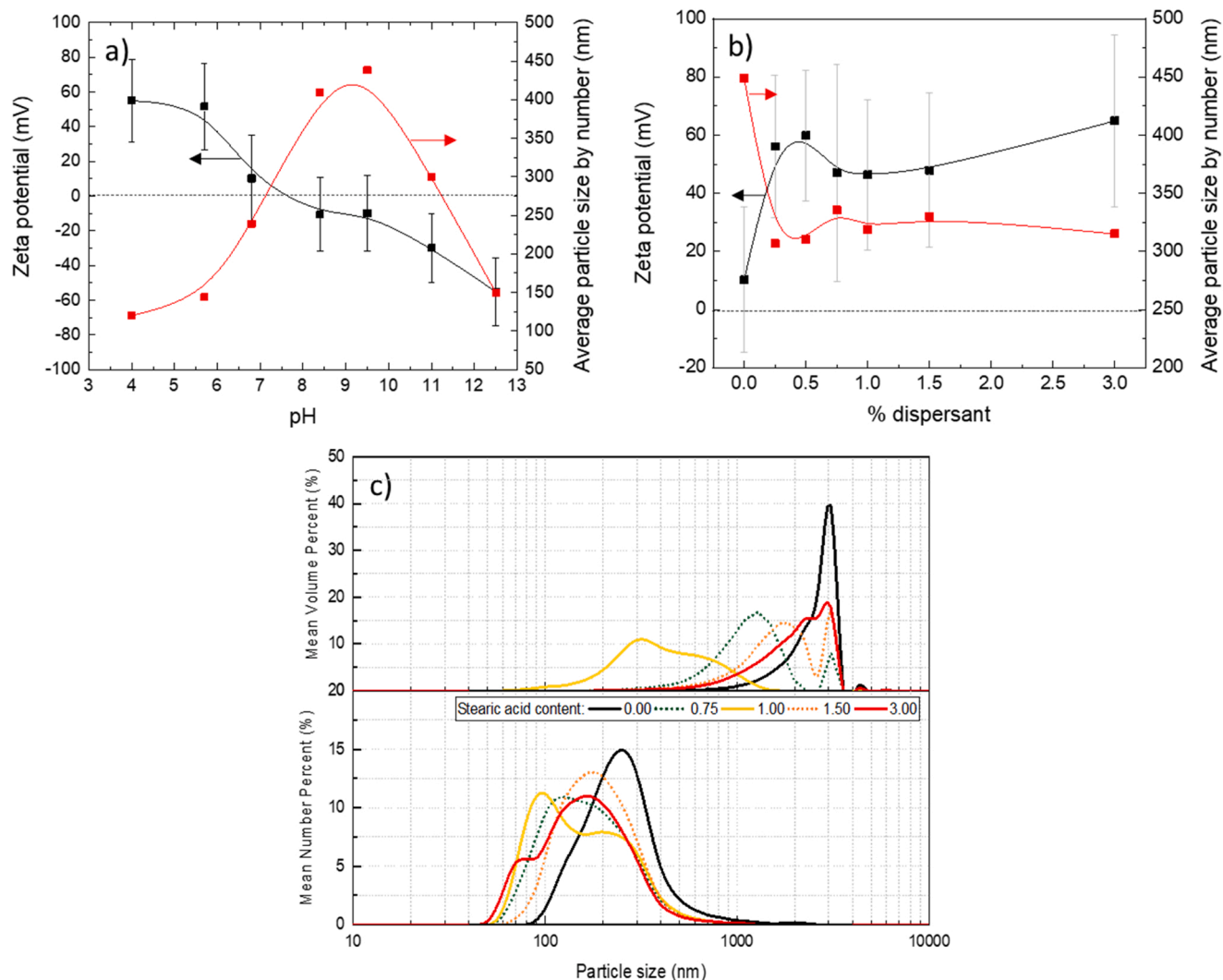
Fig. 5. Effect of the pH (a) and dispersant content (b) on the zeta potential, electric conductivity and average particle size (by number) of the Fe3Al calcined powder at pH 6. The particle size distributions (c) calculated by mean number and volume as a function of the SA addition.

x *mm* x *mm* in volume were sectioned from the top part of the sintered foams The isothermal redox performance was obtained after 10 consecutive cycles at 650, 675, and 700 °C using an alumina plate to support the porous subsample. Gas streams of Ar-10 vol% H_2 and N_2-10 vol% O_2 (using synthetic air as oxygen source) were used in the reduction and oxidation step, respectively. Sintered Fe3Al foams were heated at $50°C·min^{-1}$ under N_2 flow gas, reducing and oxidizing reaction time were both established at 12 *min*, and a N_2 flow gas was used to purge the TG between reactions for 3 *min*. Gas flow rate was established at 200 $mL·min^{-1}$ and data points were collected at a rate of 12 $data·s^{-1}$. After redox test, foams subsamples were also characterized by Mercury Intrusion Porosimetry (MIP) using a Quantachrome Poremaster 60GT porosimeter and SEM to evaluate changes in the pore structure.

3. Results and discussion

3.1. Synthesized powders characterization

Fig. 1 shows the TG and DSC curves of the as-synthesized powder with 3 wt% of Al_2O_3, in its initial gel form, (Fig. 1a) and after drying at 110 °C overnight (Fig. 1b), heating and cooling at 10°C/min. The TG curve of the gel sample showed five mayor regions of weight loss: (1) up to 149 °C, a 13.1% of weight loss was due to water and nitric acid removal, (2) at 150 ℃, the dehydroxylation of the ferric hydroxide

formed goethite (α-Fe^{3+}O(OH)) exothermally (confirmed by the exothermal peak event at the DSC curve) with a weight loss of approximately 27.2%; (3) from 150 to 203 °C, due to the decarboxylation of the organic moiety some mass was loosed (13%), the reductant atmosphere created partially reduce the Fe (III) to Fe (II) given the formation of magnetite [35], evidenced by the XRD spectrum of powder treated at 170 °C; (4) form 203–347 °C, another exothermic peak at 283 °C was detected with a weight loss of 17.3% due to the complete decomposition of the ferric citrate and goethite to form maghemite (γ-Fe_2O_3); and (5) above 400 °C a weight loos of 4.2% was noticed corresponding to complete decomposition of nitrate group and citrate precursors (under 2%), the exothermic peaks at 416 °C and 468 °C could be attributed to the oxidation of Al-citrate precursor [36] and the final formation of α-Fe_2O_3 [37], respectively.

The TG and DSC curves of the dried powder clearly showed the influence of the heat treatment due to the modification of the hydroxylation ratio, as most of the OH⁻ ions were previously removed before calcination process. Fig. 1b exhibits four regions of weight loss that could be ascribed as: (1) up to 100 °C, some water and nitrite acid remained were removed with a 1.5% of weight loss; (2) from 100 to 242 °C, another 1.0% of weight is lost due to the decarboxylation of the organic moiety; (3) from 242 to 390 °C a 3.8% of weight loss was observed with the present of exothermic peaks at 342 °C. This exothermic peak corresponds to the sequential formation of goethite to
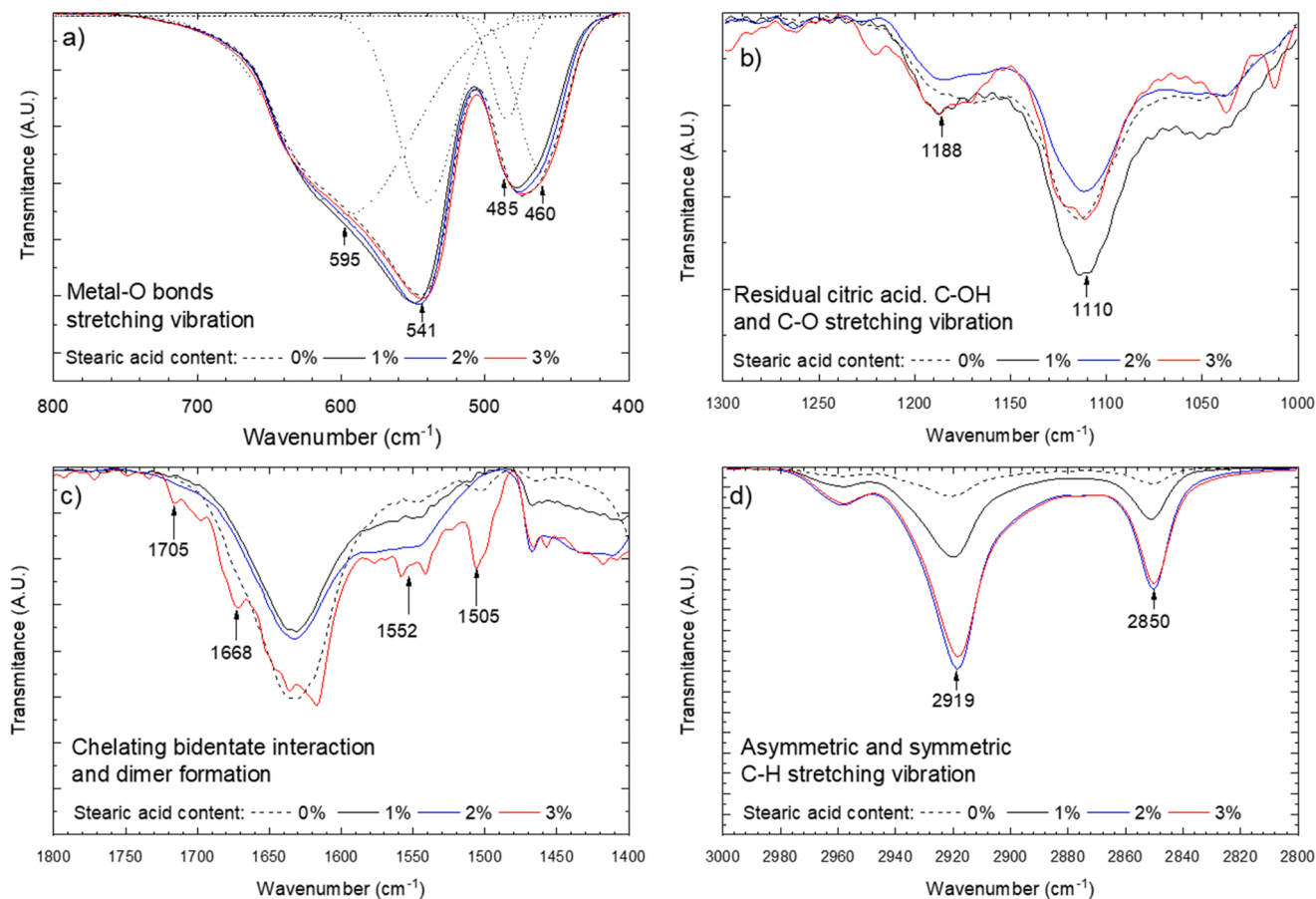
Fig. 6. FTIR spectrums at different wavenumber of Fe3Al calcined powder with different content of SA.

Table 1
Surface area, porosity and pore characterization of the Fe3Al powders with different content of SA based on Mercury intrusion porosimetry (MIP) and by N_2 adsorption/desorption characterization.

Powder feature		Stearic acid content (wt%)		
		1	2	3
BET SSA (m^2/g)		18.42	16.79	17.32
Open SSA by t-Plot (m^2/g)		23.09	22.96	23.53
Total pore SSA (m^2/g)		19.29	18.18	18.79
SSA determined by MIP (m^2/g)		21.69	23.94	20.17
Total Pore Volume (cm^3/g)	N_2	0.12	0.13	0.14
	MIP	0.79	0.51	0.59
Micropore volume by t-Plot (cm^3/g)		<0.001	0.004	0.004
Average pore (nm)	N_2	25.61	28.10	30.76
	MIP	664.7	130.4	280.1
Bulk Density by MIP (g/cm^3)		0.93	1.12	1.05
Apparent Density by MIP (g/cm^3)		3.53	2.64	2.72
Porosity (%)		73.76	57.60	60.53

Fig. 7. XRD patterns for the sintered Fe3Al foams fabricated with different content of SA: 1 (a), 2 (b), and 3 wt% (c).

α-Fe$_2$O$_3$ (hematite) [38]; (4) finally above 390 °C, a 1% of weight loss was reported when total citrate precursor with the elimination of residual carbonates occurred at 571°C [39]. No further transformation was observed beyond 620 °C.

During the TG-DSC characterization, four mayor exothermic events were observed and no mass loss was detected at a given temperature. To corroborated their effects, powder at its gel form were calcined at 170 °C, 350 °C both for 2 h and 620 °C for 6 h, heating and cooling at 10°C/min, to later perform an XRD characterization (Fig. 2).

XRD patterns in Fig. 2a and b corroborate that the exothermic peaks at 150 and 283 °C of Fig. 1a correspond to the formation of magnetite
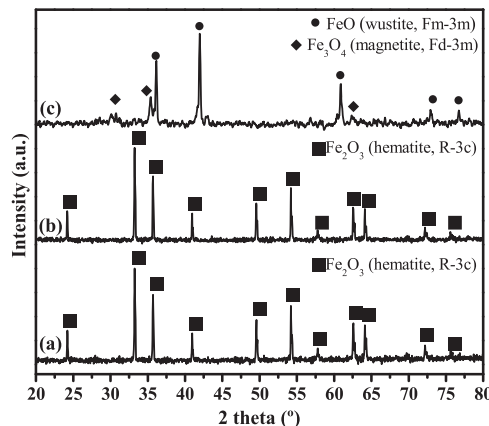
and maghemite (γ-Fe$_2$O$_3$), respectively. After calcination at 620 °C (Fig. 2c), no Al$_2$O$_3$ phase was initially distinguished due to detection limits and the low calcination temperature [39]. Therefore, the formation of hematite-like solid solution (H$_{ss}$) where Al atoms occupied cationic positions is expected [40–42]. A crystalline domain size of 46 $\pm$ 8 nm was calculated for the H$_{ss}$ phase using the Scherrer formula for all the diffraction peaks. As can be confirmed by the XRD analysis on the gel and dried powder after calcination at 620 °C for 6 h, both as-synthesized powders generate two pathways of reaction to (eventually) form the H$_{ss}$ phase.
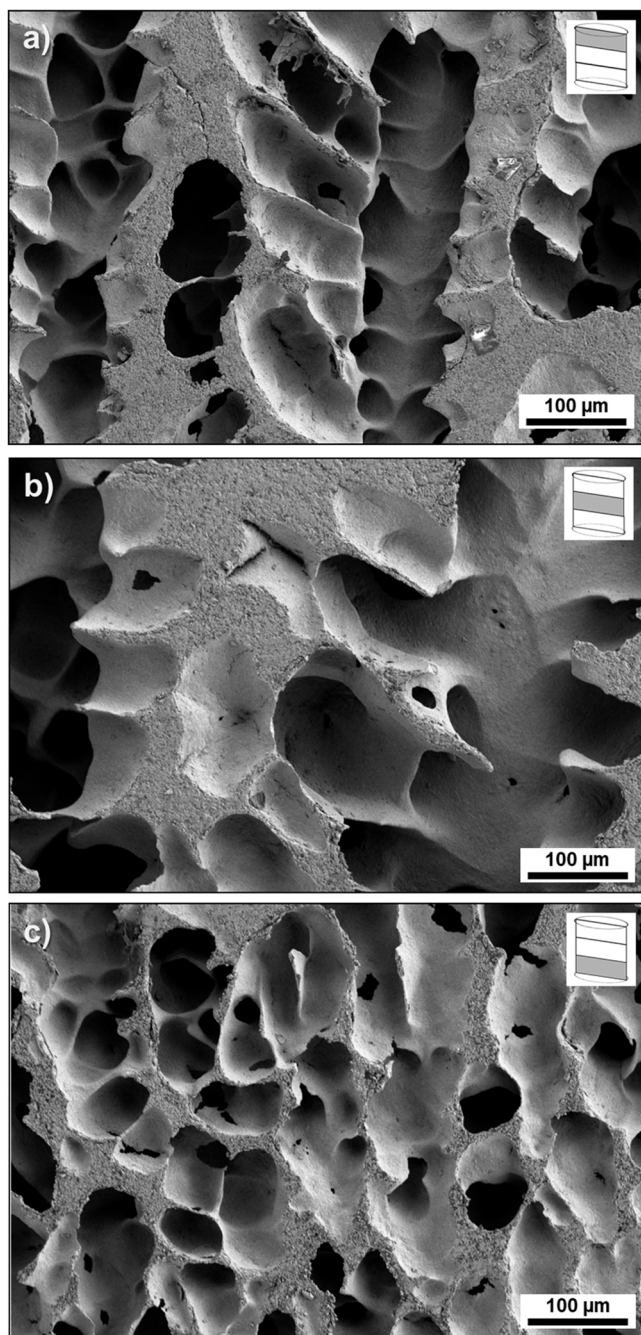
Fig. 8. SEM images of the sintered Fe3Al (with a 3 wt% of SA) foam longitudinal section at different heights: 10 mm (a), 6 mm (b), and 2 mm (c). Micrographs were taken at the axial center plane of the sample. Areas with light contrast represent the solid material.

TEM characterization of the calcined powder at 620 $°C$ showed equiaxial particles with a 37 ± 12 nm in size (Fig. 3a) calculated by image analysis (JMicrovision software), and consistent with the size value determined by XRD. A uniform distribution of Fe atoms and Al atoms colonies scattered at the particle surface (Fig. 3b) is also evidenced. High-resolution XPS spectra (Fig. 4) show the valence state and compositional studies of Fe, Al, and O of the Fe3Al and Fe0Al synthesized powder. The XPS spectra of Fe 2p of Fe3Al powder in Fig. 4a showed two major peaks at 710.9 and 724.2 eV identified with the Fe^{3+} ions assigned to Fe $2p_{3/2}$ and Fe $2p_{1/2}$ respectively, and satellite peaks were also identified at 718.6 and 732.6 eV. The major peaks were separated by a spin energy of 13.3 eV, while the associated satellite of

the Fe $2p_{3/2}$ peak was at 7.7 eV, both values were in good agreement with the reported value for α-Fe_2O_3 in the literature [43,44]. The influence of the Al atoms in hematite solid solution was also visible as the spectra of Fe 2p on the Fe3Al powder has moved to slightly higher binding energy (+0.8 eV) as compared with the Fe0Al powder (Fig. 4a). The ionic nature of the Al-O bond, in respect to the Fe-O covalent bond, might be responsible for the increased in the binding energy observed in the Fe3Al powder. The binding energy of Al^{3+} as metal, within a $FeAl_2O_4$ phase, and in Al_2O_3 phase are 73.0 eV, 74.5 eV, and 75.8 eV respectively [45], and the XPS spectrum of Al 2p of Fig. 4b showed a binding energy of 75.4 eV corresponding to cation position in Al_2O_3 phase in concordance with the TEM observation. The XPS spectrum of O 1 s of the Fe3Al powder (Fig. 4c) shows a single peak at 530.1 eV (+0.7 eV of the Fe0Al powder) broaden to higher binding energies due to the influence of the Al cations, as Al atoms occupy cation position in the H_{ss}, the O 1 s also moves to higher binding energies respectively [45]. Finally, the synthesized Fe3Al powder crystallized as α-Fe_2O_3 in a hematite-like Al solid solution.

Fig. 5a shows the influence of pH on the zeta potential and average particle size obtained as the mean value determined from the particle size distribution in number of the Fe3Al calcined powders. The measurements were made at pH 4 since below pH 3.5 the Poubaix diagram predicts the dissolution of the hematite. The zeta potential of the Fe3Al powder moves from 56 to −55 mV for pH values ranging 4–12.5, with an isoelectric point at pH 7.5. The average particle size (estimated by number) shows values of 120 nm and 150 nm at pH 4 and 12.5, respectively. At pH 6 with a zeta potential of 56 mV, the measured particle size was 150 nm, while at pH 7 zeta potential decreases below 20 mV as particle size slightly increases. Therefore, this pH range (6−7) was selected to overview the influence of the dispersant content, since under hydroxyl group of the SA could be slightly deprotonated and negatively charged. Fig. 5b shows the influence of the dispersant content (SA) over the zeta potential and particle size of Fe3Al powder suspended in ethanol. As the SA content increases over 0.5 wt%, the zeta potential and the particle size stabilise around 50–60 mV and 300 nm, respectively. It has been reported that SA is anchored to the particle by their carboxylic group [46], favouring the steric repulsion among Fe3Al nanoparticles that maintain them dispersed. From 1–3 wt% of SA, although no significant change in the zeta potential and the particle size were detected, most likely due to the maximum Fe3Al particle coverage produced by the SA, a slight upturn of the zeta potential can be intuited for a 3 wt%.

The influence of the SA in the stability was explored in detail by comparing the particle size distributions in number and volume (Fig. 5c). The particle size distribution in volume shows a maximum reduction at 1 wt% of SA with a mean value of 330 nm. In fact, with no SA added, the Fe3Al particle were poorly dispersed and formed agglomerates of about 3000 nm, but as the SA was incorporated and adsorbed by the particle, their size diminished significantly. Beyond 1 wt% of SA (curves at 1.5 and 3 wt% of SA), Fe3Al particles seem to re-aggregate progressively forming groups of particles above the 2 μm. This behavior could be related to an interaction between the adsorbed and dissolved SA molecules acting as binder-bridges that increases the particle size, as have been observed for Fe_3O_4 coated with oleic acid [47], a similar fatty acid compound. However, these results must be complemented with the particle size distribution in number, as wide size distribution could be deceived due to the low contribution of the smaller particle to the cumulate volume curve. At the size distribution by number, curves showed similar behavior despite the SA content, being the majority of the particles under 400 nm. With SA addition particle size distribution moves to lower sizes until 1 wt%, with a considerable among of particle below 100 nm then, as the SA content keep rising, distribution curves moves back to higher particle size with no significant number of particles over 1μm. Therefore, the Fe3Al powder with 3 wt% of SA as dispersant agent showed a broad particle size distribution with an average diameter of 150 nm, that is with an agglomeration factor
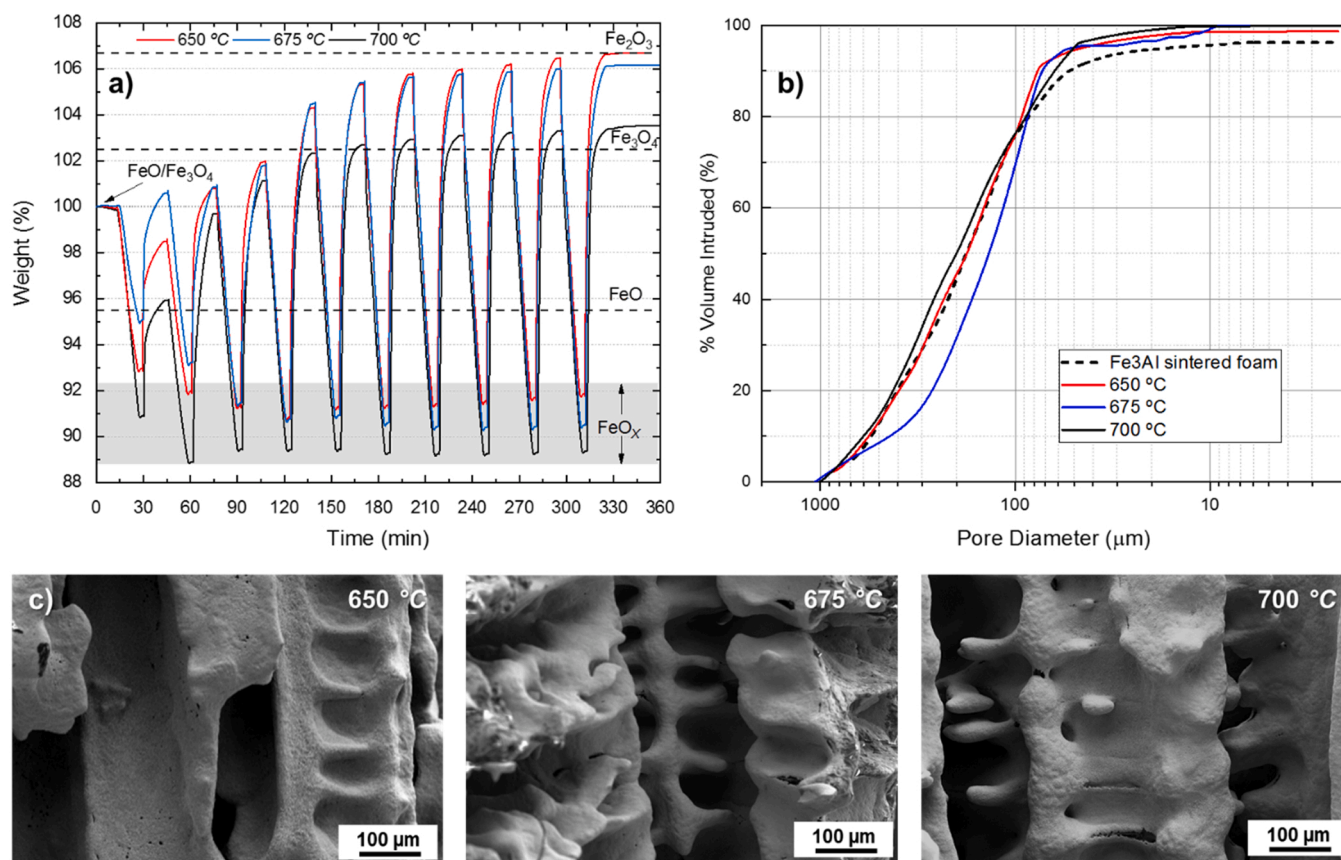
Fig. 9. TG analysis (a), MIP curves of volume intruded percentage (%) versus pore diameter (b), and SEM images (c) at the axial plane of the sintered Fe3Al foams after 10 redox cycles at different temperature (650, 675, and 700 ℃). Stoichiometry mass of FeO, Fe₃O₄, and Fe₂O₃ phase (a), and initial volume intruded percentage curve of the sintered Fe3Al foams (b) were included as guideline and comparison in dotted lines.

(Fag=D_{V50}/D_{TEM}) of 3 since the initial particle size is about 50 *nm*.

The FTIR spectra of Fe3Al calcined powder at 620 ℃ further dispersed with 0, 1, 2, and 3 wt% of SA are shown in Fig. 6. Between 800 cm^{-1} and 400 cm^{-1} bands in Fig. 6a, four overlapped peaks (dotted lines) were determined after Gaussian deconvolution due to the oxygen bonds with Fe and Al metal cations in the hematite-like Al solid solution. These peaks were identified at lower wavenumber compared to the literature. Fe-O bonds showed stretching vibrations at 541 cm^{-1} and 460 cm^{-1} [48], while the Al-O bonds showed stretching-vibrational at 595 cm^{-1} and 485 cm^{-1} [49]. Moreover in Fig. 6b, a band attributable to -C-OH stretching appeared at 1110 cm^{-1} and -C-O stretching located at 1188 cm^{-1} due to some residual citric acid [50].

At Fig. 6c, the powders showed a band at 1638–1618 cm^{-1} corresponding to the bending vibrations of the surface hydroxyl group [47]. No peak at 1700–1715 cm^{-1} was determined at 0–2 wt% of SA corresponding to the carboxylic group due to the formation of a single coating layer around the Fe3Al particles bonded by the carboxylic group [47]. However, at 3 wt% of SA the following features were observed: (1) a peak at 1705 cm^{-1} is slightly appeared due to the formation of a multi-layer around the particles [47,51]; (2) the two characteristic peaks at 1668 cm^{-1} and 1552 cm^{-1} belong to the symmetric and asymmetric carboxylate group stretching band, $\upsilon_{(COO-)asym}$ and $\upsilon_{(COO-)sym}$ respectively, due to the chelating bidentate interaction between carboxylate groups and metal sites [47,52], and 3) the appeared of a new peak at 1505 cm^{-1}. This new peak could be attributed to the SA molecule forming dimers with the free molecule or along coated particles [53] acting as a binder. The absorption peaks at about 2919 and 2850 cm^{-1} in the high-frequency region (Fig. 6d) were attributed to $-CH_2-$ band asymmetric and symmetric stretching vibrations of SA, respectively. These peaks were more intense as the SA content increased.

The dimers and the chelating interactions might be responsible for the enhancement of green strength observed in the Fe3Al foam with 3 wt % of SA, as they might be acting as a binder agent, since slurries with 1 and 2 wt% of SA were also created to manufacture Fe3Al foams according to Section 2.2, but the samples crumbled after de-moulding and camphene removal. Also, the slurry with 1 wt% of SA showed high viscosity and was difficult to pour into the mould, which could be linked to the significant number of particles under 100 *nm* observed in Fig. 5c.

Table 1 collects the main morphological properties of the Fe3Al powders with different content of SA from the green sample after been resulting from the porosity exploration. N₂ adsorption/desorption data analysis evidences a wide specific surface area (SSA) of the shaped parts (>10 m^2/g), with a total absence of microporosity. The BET surface area and open SSA maintains around 17 and 23 m^2/g, respectively, exhibiting lower values for the 2 wt% SA powder. However, the SSA determined by MIP ranges 20–24 m^2/g, having the highest value (23.94 m^2/g) this of the Fe3Al 2 wt% SA powder.

In all powder samples, the total pore volume is higher for the range of pores determined by MIP (0.51–0.79 cm^3/g) than for porosity determined by N₂ adsorption/desorption (0.12–1.14 cm^3/g), and consequently the large mesopososity has a higher contribution to the porous structure. Main porosity determined by those techniques, N₂ adsorption/desorption and MIP, are in the range of 31–26 *nm* and 665–130 *nm*, respectively. Differences in SSA, volume and size of pores suggest qualitative and quantitative differences in the porous microstructures only depending on the particles stabilization/surface modification and/ or the bider role of SA. The powder prepared from particles dispersed with 1 wt% of SA, exhibits the highest porosity (73.76%) with pores ranging from 665 *nm* to 23 *nm*. The addition of 2 wt% of SA to stabilize the nanoparticles suspension leads to a less porous microstructure

(57.60% of porosity) with the smaller and narrower pore size distribution (130–24 *nm*), evidencing the role of binder of the amount of SA added in excess. With the addition of 3 wt% of SA, the powder exhibits a relative similar porosity (60.53%) than with 2 wt% of SA, with large pores in both ranges: 280 *nm* determined by MIP and 30.76 *nm* determined by N_2 adsorption/desorption, but with higher apparent density by MIP.

The bulk density increases as SA content increases, which is in line with the mechanical stability of foams shaped after the evaporation of the camphene. The Fe3Al powders processed with 3 wt% of SA is the only material maintaining its shape after freezing. The increase of bulk density and mechanical stability is also in line with the decrease in the pore size of powders processed with 2 and 3 wt%. On the other hand, the apparent density can be considered equivalent to the density of the powder skeleton, the density of the material to which mercury does not have access. This density is higher when the nanoparticles are better dispersed (with 1 wt% SA), but the low solids content considered and the high rheology of the suspension will make the material lack physical integrity. Powders processed with 2 and 3 wt% SA have lower apparent densities, and it is the effect of the binder that will allows the foam to maintain its mechanical integrity after drying, with a lower volume and size of pores. Therefore, the combining effects of the higher bulk density, medium porosity and the seemingly binder properties of the SA, could explain the high performance of foams after freezing when using suspensions stabilized with a 3 wt%. Structural stability of Fe3Al foams obtained with 3 wt% of SA makes them optimum to be used to fabricate the sintered foams.

3.2. Doped Fe_2O_3 foam characterization

The XRD analysis performed over the sintered Fe3Al foams prepared with 1, 2 and 3 wt% of SA (Fig. 7) shows significant results. The use of 3 wt% of SA produced a reduction of the Fe_2O_3 phase to a combination of FeO and Fe_3O_4 phases, when lower SA content (1 and 2 wt% of SA) did not produce any hematite reduction. According to the literature, the use of up to 3 wt% Al_2O_3 enhances the reduction process of Fe_3O_4 due to the formation of a network-like structure of FeO [54,55]. These studies employed a CO-CO_2 gas stream as a reductant source, but here sintering process was performed in a close cylindrical furnace, being the only reductant source, the carbon atoms present in the SA molecules ($C_{18}H_{36}O_2$). Reduction of iron oxide via organic compounds have been reported previously [56]. But, it was not observed in similar research when polystyrene $((C_8H_8)_{n-1})$ and oligomeric polyester ($C_{90}H_{172}O_{10}$) were used as binder and dispersant agent, respectively [24]. In this case, the reduction process might be enhanced due to the local concentration of organic compound via the covering of the Fe3Al powder by SA molecules and the presence of higher Al_2O_3 content. Quantitative phase analysis was performed by Rietveld analysis over the sintered Fe3Al foam with 3 wt% of SA where a 77.2 and 22.8 wt% of FeO and Fe_3O_4 phases were respectively, determined.

As for the foam pore structure, the cooling system employed in this research generates a directional solidification with a non-constant cooling rate where the thermal gradient decreased, and the solidification front velocity increased throughout the sample height [57]. This cooling procedure promotes significant differences in pore morphology along the cooling direction, as it is shown in Fig. 8. The SEM images were taken at the axial central plane of the sintered Fe3Al (with a 3 wt% of SA) foam display a significant branched pore structure at the bottom part, while the rest of the sample shows pores with a well-defined dendritic shape. These different pore structures were promoted by the use of nanometric powder and the variation of the cooling rate throughout the sample height.

At the lower part of the samples (near the mould bottom), the rapid cooling produces the rapid formation of a camphene solidification front. The nucleation and growth of numerous dendritic crystals impinging each other have created an interconnected solid structure that has

pushed the particles to the interdendritric spaces (Fig. 8c). As the solidification front moves within the sample (middle and top part), the reduction of the thermal gradient increases the solidification front velocity leading to elongated camphene dendrites (Fig. 8b) with well-defined secondary arms (Fig. 8a). The average pore diameters, estimated by image analysis, were 170 ± 15, 199 ± 18, and $126 \pm 17 \mu m$ in areas described by Fig. 8a–c, respectively. The density of the sample was estimated by Archimedes method on 1.24 $g \cdot cm^{-3}$ with an open and close porosity of 75.0% and 1.3%, respectively. The use of SA reduced the aggregate size of the synthesized powder dispersed in camphene improving the dendrite contour replication during solidification and increasing the pore size. This improvement is based on the increase of the critical velocity for particle engulfment (V_{cr}) proposed by Stefanescu [58] which is roughly $V_{cr} \approx 1/D$ (being D the particle diameter), below this velocity particles are pushed rather than trapped by the solidification front. Therefore, camphene crystal could grow by pushing the particles within a much wider range of velocity, also reproducing the dendrite contour much better.

3.3. Redox performance of the sintered Fe3Al foam

According to Rietveld of the XRD diffraction in Fig. 7, the sintered Fe3Al foam with 3 wt% of SA presented a 77.2 wt% of FeO and 22.8 wt% of Fe_3O_4. Therefore, if complete reduction of the foams were achieved a 74.2% of mass reduction would be obtained. In turn since the oxidation step was performed in air due to experimental limitation, the complete oxidation of Fe would create Fe_2O_3 with a mass gain of 106.3%. Fig. 9a showed the TG analysis of the sintered Fe3Al foams during 10 isothermal redox cycles. A full reduction was not achieved at any tested temperature due to the duration of the reduction step, instead an over oxidation was recorded due to the use of synthetic air. Foams retained their redox performance during cycling, as they gained weight in all cases, reaching faster a steady-state when operando temperature decreases.

According to the literature [59,60], hematite follows a two-step reduction process where on the first step Fe_2O_3 reduces to Fe_3O_4, at the second step, Fe_3O_4 is reduced directly to Fe or forms FeO as a transition phase. In this case (Fig. 9a), samples were partially reducing to a FeO_X phase with X being approximately 0.79, 0.75, and 0.69 for 650, 675, and 700 °C, respectively. During reoxidation, the use of O_2 promotes the direct formation of Fe_2O_3 phase, while steam will only promote the generation of Fe_3O_4 phase due to thermodynamic restriction. Therefore, the mass gained up to stoichiometry mass of Fe_3O_4 phase will correspond to a hydrogen production if a steam flow had been employed. At 700 °C, TG analysis (Fig. 9a) shows the highest degree of reduction and, at the re-oxidation step, the stoichiometry mass line of the Fe_3O_4 phase is overpassed at all operando temperatures. These results suggest that Fe3Al foams are able to produce hydrogen with the use of steam with no reduction in redox performance during the redox cycling.

Regarding the pore size and morphology, no significant variation on the cumulated volume intruded curves were observed before and after redox test (Fig. 9b). Pore diameter at 50% of volume intruded were estimated in 160–200 μm for sintered samples before and after redox test, those values are in good correlation with results obtained by image analysis on Section 3.2. Also, the SEM image analysis on Fig. 9c reveals not significant changes as compared by initial pore morphology on Fig. 8a, and dendritic contours are retained after the redox cycles at all temperature. This is especially interesting, as foams recover all the weight during oxidation, gain further more mass until full re-oxidation, and showed no sign of performance reduction or structural degradation.

4. Conclusions

Hematite foams have been successfully developed by freeze-casting for redox applications. The synthesis of the nanometric powder by

coprecipitation, and the use of SA as dispersant/binder agent results in the production of foams with pore sizes over 100 μm with enhanced dendritic contour definition. SA has a relevant role structurer, and also acts as a reductant agent over the hematite nanoparticles. Sintered foams were able to withstand 10 redox cycles with adequate performance as no significant effect on the porosity was observed. The comparison of the hydrogen production with the oxidation reaction seems valid and useful, as the gain weight was over the stoichiometry value of the Fe_3O_4 with no structural degradation of the foams. Future works will focus in testing a higher number of redox cycles within a wider range of temperature and using steam as oxidizing gas.

Declaration of Competing Interest

The authors declare that they have no known competing financial interests or personal relationships that could have appeared to influence the work reported in this paper.

Acknowledgements

References

[1] L. Al-Ghussain, Global warming: review on driving forces and mitigation, Environ. Prog. Sustain Energy 38 (2019) 13–21, https://doi.org/10.1002/ep.13041.

[2] P. Nikolaidis, A. Poullikkas, A comparative overview of hydrogen production processes, Renew. Sustain. Energy Rev. 67 (2017) 597–611, https://doi.org/10.1016/j.rser.2016.09.044.

[3] S.E. Hosseini, M.A. Wahid, Hydrogen production from renewable and sustainable energy resources: promising green energy carrier for clean development, Renew. Sustain Energy Rev. 57 (2016) 850–866, https://doi.org/10.1016/j.rser.2015.12.112.

[4] M. Shahbaz, S. Yusup, A. Inayat, D.O. Patrick, M. Ammar, The influence of catalysts in biomass steam gasification and catalytic potential of coal bottom ash in biomass steam gasification: a review, Renew. Sustain Energy Rev. 73 (2017) 468–476, https://doi.org/10.1016/j.rser.2017.01.153.

[5] R. Zacharias, S. Visentin, S. Bock, V. Hacker, High-pressure hydrogen production with inherent sequestration of a pure carbon dioxide stream via fixed bed chemical looping, Int. J. Hydrog. Energy 44 (2019) 7943–7957, https://doi.org/10.1016/j.ijhydene.2019.01.257.

[6] X. Zhu, M. Zhang, K. Li, Y. Wei, Y. Zheng, J. Hu, et al., Chemical-looping water splitting over ceria-modified iron oxide: Performance evolution and element migration during redox cycling, Chem. Eng. Sci. 179 (2018) 92–103, https://doi.org/10.1016/j.ces.2018.01.015.

[7] E. Hormilleja, P. Durán, J. Plou, J. Herguido, J.A. Peña, Hydrogen from ethanol by steam iron process in fixed bed reactor, Int. J. Hydrog. Energy 39 (2014) 5267–5273, https://doi.org/10.1016/j.ijhydene.2014.01.002.

[8] P. De Filippis, L. D'Alvia, M. Damizia, B. Caprariis, Z. Del Prete, Pure hydrogen production by steam-iron process: the synergic effect of MnO_2 and Fe_2O_3, Int. J. Energy Res. 45 (2021) 4479–4494, https://doi.org/10.1002/er.6117.

[9] R. Chaubey, S. Sahu, O.O. James, S. Maity, A review on development of industrial processes and emerging techniques for production of hydrogen from renewable and sustainable sources, Renew. Sustain Energy Rev. 23 (2013) 443–462, https://doi.org/10.1016/j.rser.2013.02.019.

[10] J. Saupsor, S. Wongsakulphasatch, P. Kim-Lohsoontorn, P. Bumroongsakulsawat, W. Kiatkittipong, S. Ratchahat, et al., Fe_2O_3/CaO-Al_2O_3 multifunctional catalyst for hydrogen production by sorption-enhanced chemical looping reforming of ethanol, Biomass Convers. Biorefin. (2020), https://doi.org/10.1007/s13399-020-00947-z.

[11] G. Voitic, V. Hacker, Recent advancements in chemical looping water splitting for the production of hydrogen, RSC Adv. 6 (2016) 98267–98296, https://doi.org/10.1039/C6RA21180A.

[12] J. Zou, J. Oladipo, S. Fu, A. Al-Rahbi, H. Yang, C. Wu, et al., Hydrogen production from cellulose catalytic gasification on CeO_2/Fe_2O_3 catalyst, Energy Convers. Manag 171 (2018) 241–248, https://doi.org/10.1016/j.enconman.2018.05.104.

[13] Y. Zhang, E. Doroodchi, B. Moghtaderi, J. Plou, P. Durán, J. Herguido, et al., Über das Ausfrieren von Hydrosolen, Int J. Hydrog. Energy 35 (2012) 278–290, https://doi.org/10.1007/BF01412789.

[14] A. Gholizadeh, The effects of A/B-site substitution on structural, redox and catalytic properties of lanthanum ferrite nanoparticles, J. Mater. Res. Technol. 8 (2019) 457–466, https://doi.org/10.1016/j.jmrt.2017.12.006.

[15] M. Ismail, W. Liu, M.T. Dunstan, S.A. Scott, Development and performance of iron based oxygen carriers containing calcium ferrites for chemical looping combustion and production of hydrogen, Int. J. Hydrog. Energy 41 (2016) 4073–4084, https://doi.org/10.1016/j.ijhydene.2015.11.066.

[16] Z. Sun, S. Chen, C.K. Russell, J. Hu, A.H. Rony, G. Tan, et al., Improvement of H_2-rich gas production with tar abatement from pine wood conversion over bi-functional $Ca_2Fe_2O_5$ catalyst: Investigation of inner-looping redox reaction and promoting mechanisms, Appl. Energy 212 (2018) 931–943, https://doi.org/10.1016/j.apenergy.2017.12.087.

[17] W. Liu, M. Ismail, M.T. Dunstan, W. Hu, Z. Zhang, P.S. Fennell, et al., Inhibiting the interaction between FeO and Al_2O_3 during chemical looping production of hydrogen, RSC Adv. 5 (2015) 1759–1771, https://doi.org/10.1039/C4RA11891J.

[18] K. Otsuka, T. Kaburagi, C. Yamada, S. Takenaka, Chemical storage of hydrogen by modified iron oxides, J. Power Sources 122 (2003) 111–121, https://doi.org/10.1016/S0378-7753(03)00398-7.

[19] D.-W. Zeng, S. Peng, C. Chen, J.-M. Zeng, S. Zhang, H.-Y. Zhang, et al., Nanostructured Fe_2O_3/$MgAl_2O_4$ material prepared by colloidal crystal templated sol–gel method for chemical looping with hydrogen storage, Int. J. Hydrog. Energy 41 (2016) 22711–22721, https://doi.org/10.1016/j.ijhydene.2016.09.180.

[20] Z. Huang, Z. Deng, D. Chen, G. Wei, F. He, K. Zhao, et al., Exploration of reaction mechanisms on hydrogen production through chemical looping steam reforming using $NiFe_2O_4$ oxygen carrier, ACS Sustain. Chem. Eng. 7 (2019) 11621–11632, https://doi.org/10.1021/acssuschemeng.9b01557.

[21] R. Zacharias, S. Bock, V. Hacker, The impact of manufacturing methods on the performance of pelletized, iron-based oxygen carriers for fixed bed chemical looping hydrogen in long term operation, Fuel Process Technol. 208 (2020), 106487, https://doi.org/10.1016/j.fuproc.2020.106487.

[22] S. Zhang, Y. Feng, X. Guo, Redox performance of Cu-doped Fe_2O_3/Al_2O_3 as oxygen carriers for chemical looping hydrogen production, Energy Fuels 35 (2021) 626–635, https://doi.org/10.1021/acs.energyfuels.0c03496.

[23] P.R. Kidambi, J.P.E. Cleeton, S.A. Scott, J.S. Dennis, C.D. Bohn, Interaction of iron oxide with alumina in a composite oxygen carrier during the production of hydrogen by chemical looping, Energy Fuels 26 (2012) 603–617, https://doi.org/10.1021/ef200859d.

[24] P.J. Lloreda-Jurado, J. Hernández-Saz, E. Chicardi, A. Paúl, R. Sepúlveda, Pore morphology evolution and atom distribution of doped Fe_2O_3 foams developed by freeze-casting after redox cycling, J. Mater. Res. Technol. 13 (2021) 1887–1898, https://doi.org/10.1016/j.jmrt.2021.06.008.

[25] Y. Long, K. Li, Z. Gu, X. Zhu, Y. Wei, C. Lu, et al., Ce-Fe-Zr-O/MgO coated monolithic oxygen carriers for chemical looping reforming of methane to co-produce syngas and H_2, Chem. Eng. J. 388 (2020), 124190, https://doi.org/10.1016/j.cej.2020.124190.

[26] P. Durán, J. Lachén, J. Plou, R. Sepúlveda, J. Herguido, J.A. Peña, Behaviour of freeze-casting iron oxide for purifying hydrogen streams by steam-iron process, Int. J. Hydrog. Energy 41 (2016) 19518–19524, https://doi.org/10.1016/j.ijhydene.2016.06.062.

[27] W.L. Li, K. Lu, J.Y. Walz, Freeze casting of porous materials: review of critical factors in microstructure evolution, Int. Mater. Rev. 57 (2012) 37–60, https://doi.org/10.1179/1743280411Y.0000000011.

[28] I. Nelson, S.E. Naleway, Intrinsic and extrinsic control of freeze casting, J. Mater. Res. Technol. 8 (2019) 2372–2385, https://doi.org/10.1016/j.jmrt.2018.11.011.

[29] S.K. Wilke, D.C. Dunand, Structural evolution of directionally freeze-cast iron foams during oxidation/reduction cycles, Acta Mater. 162 (2019) 90–102, https://doi.org/10.1016/j.actamat.2018.09.054.

[30] T. Um, S.K. Wilke, H. Choe, D.C. Dunand, Effects of pore morphology on the cyclical oxidation/reduction of iron foams created via camphene-based freeze casting, J. Alloy. Compd. (2020), 156278, https://doi.org/10.1016/j.jallcom.2020.156278.

[31] P.J. Lloreda-Jurado, S.K. Wilke, K. Scotti, A. Paúl-Escolano, D.C. Dunand, R. Sepúlveda, Structure–processing relationships of freeze-cast iron foams fabricated with various solidification rates and post-casting heat treatment, J. Mater. Res. (2020) 1–10, https://doi.org/10.1557/jmr.2020.175.

[32] E. Lorente, J.A. Peña, J. Herguido, Separation and storage of hydrogen by steam-iron process: effect of added metals upon hydrogen release and solid stability, J. Power Sources 192 (2009) 224–229, https://doi.org/10.1016/j.jpowsour.2008.12.116.

[33] P.J. Lloreda-Jurado, V. Perez-Puyana, A. Romero, R. Sepúlveda, Influences of the solid load on the microstructure and compressive behavior of Fe_2O_3 scaffolds manufactured by freeze-casting using stearic acid as dispersant agent, J. Eur. Ceram. Soc. 42 (2022) 193–201, https://doi.org/10.1016/j.jeurceramsoc.2021.09.056.

[34] T. Hildebrand, P. Rüegsegger, A new method for the model-independent assessment of thickness in three-dimensional images, J. Microsc. 185 (1997) 67–75, https://doi.org/10.1046/j.1365-2818.1997.1340694.x.

[35] X. Liu, Y. Guo, Y. Wang, J. Ren, Y. Wang, Y. Guo, et al., Direct synthesis of mesoporous Fe3O4 through citric acid-assisted solid thermal decomposition, J. Mater. Sci. 45 (2010) 906–910, https://doi.org/10.1007/s10853-009-4019-1.

[36] P. Suhasinee Behera, S. Bhattacharyya, R. Sarkar, Effect of citrate to nitrate ratio on the sol-gel synthesis of nanosized α-Al2O3 powder, Ceram. Int. 43 (2017) 15221–15226, https://doi.org/10.1016/j.ceramint.2017.08.057.

[37] E. Tronc, J.P. Jolivet, J. Livage, Mössbauer investigation of the γ→α-Fe_2O_3 transformation in small particles, Hyperfine Interact. 54 (1990) 737–740, https://doi.org/10.1007/BF02396121.

[38] P. Melnikov, V.A. Nascimento, I.V. Arkhangelsky, L.Z. Zanoni Consolo, L.C.S. de Oliveira, Thermal decomposition mechanism of iron(III) nitrate and characterization of intermediate products by the technique of computerized

modeling, J. Therm. Anal. Calorim. 115 (2014) 145–151, https://doi.org/10.1007/s10973-013-3339-1.

[39] J. Li, Y. Pan, C. Xiang, Q. Ge, J. Guo, Low temperature synthesis of ultrafine α-Al_2O_3 powder by a simple aqueous sol–gel process, Ceram. Int. 32 (2006) 587–591, https://doi.org/10.1016/j.ceramint.2005.04.015.

[40] A.K. Ladavos, T.V. Bakas, The Al_2O_3-Fe_2O_3 mixed oxidic system, I. Preparation and characterization, React. Kinet. Catal. Lett. 73 (2001) 223–228, https://doi.org/10.1023/A:1014134601603.

[41] V. Raghavan, Al-Fe-O (aluminum-iron-oxygen), J. Phase Equilibria Diffus 31 (2010) 367, https://doi.org/10.1007/s11669-010-9712-x.

[42] A.C. Turnock, H.P. Eugster, Fe–Al oxides: phase relationships below 1,000C, J. Pet. 3 (1962) 533–565, https://doi.org/10.1093/petrology/3.3.533.

[43] X.-F. Lu, X.-Y. Chen, W. Zhou, Y.-X. Tong, G.-R. Li, α-Fe_2O_3 @PANI core–shell nanowire arrays as negative electrodes for asymmetric supercapacitors, ACS Appl. Mater. Interfaces 7 (2015) 14843–14850, https://doi.org/10.1021/acsami.5b03126.

[44] T. Yamashita, P. Hayes, Analysis of XPS spectra of Fe^{2+} and Fe^{3+} ions in oxide materials, Appl. Surf. Sci. 254 (2008) 2441–2449, https://doi.org/10.1016/j.apsusc.2007.09.063.

[45] A. Velon, I. Olefjord, Oxidation behavior of Ni_3Al and Fe_3Al: I. XPS calibrations of pure compounds and quantification of the results, Oxid. Met. 56 (2001) 415–424, https://doi.org/10.1023/A:1012589315800.

[46] S. Zürcher, T. Graule, Influence of dispersant structure on the rheological properties of highly-concentrated zirconia dispersions, J. Eur. Ceram. Soc. 25 (2005) 863–873, https://doi.org/10.1016/j.jeurceramsoc.2004.05.002.

[47] H.T. Ong, D.D. Suppiah, N. Muhd Julkapli, Fatty acid coated iron oxide nanoparticle: effect on stability, particle size and magnetic properties, Colloids Surf. A Physicochem Eng. Asp. 606 (2020), 125371, https://doi.org/10.1016/j.colsurfa.2020.125371.

[48] S. Nag, A. Roychowdhury, D. Das, S. Mukherjee, Synthesis of α-Fe_2O_3-functionalised graphene oxide nanocomposite by a facile low temperature method and study of its magnetic and hyperfine properties, Mater. Res. Bull. 74 (2016) 109–116, https://doi.org/10.1016/j.materresbull.2015.10.017.

[49] G. Zu, J. Shen, X. Wei, X. Ni, Z. Zhang, J. Wang, et al., Preparation and characterization of monolithic alumina aerogels, J. Non Cryst. Solids 357 (2011) 2903–2906, https://doi.org/10.1016/j.jnoncrysol.2011.03.031.

[50] J. Li, Y. Wu, M. Yang, Y. Yuan, W. Yin, Q. Peng, et al., Electrospun Fe_2O_3 nanotubes and Fe_3O_4 nanofibers by citric acid sol-gel method, J. Am. Ceram. Soc. 100 (2017) 5460–5470, https://doi.org/10.1111/jace.15164.

[51] N.V. Jadhav, A.I. Prasad, A. Kumar, R. Mishra, S. Dhara, K.R. Babu, et al., Synthesis of oleic acid functionalized Fe_3O_4 magnetic nanoparticles and studying their interaction with tumor cells for potential hyperthermia applications, Colloids Surf. B Biointerfaces 108 (2013) 158–168, https://doi.org/10.1016/j.colsurfb.2013.02.035.

[52] J. Liang, H. Li, J. Yan, W. Hou, Demulsification of oleic-acid-coated magnetite nanoparticles for cyclohexane-in-water nanoemulsions, Energy Fuels 28 (2014) 6172–6178, https://doi.org/10.1021/ef501169m.

[53] S.R. Mihajlović, D.R. Vučinić, Ž.T. Sekulić, S.Z. Milićević, B.M. Kolonja, Mechanism of stearic acid adsorption to calcite, Powder Technol. 245 (2013) 208–216, https://doi.org/10.1016/j.powtec.2013.04.041.

[54] Y. Kapelyushin, Y. Sasaki, J. Zhang, S. Jeong, O. Ostrovski, In-situ study of gaseous reduction of magnetite doped with alumina using high-temperature XRD analysis, Met. Mater. Trans. B 46 (2015) 2564–2572, https://doi.org/10.1007/s11663-015-0437-4.

[55] Y. Kapelyushin, Y. Sasaki, J. Zhang, S. Jeong, O. Ostrovski, Formation of a network structure in the gaseous reduction of magnetite doped with alumina, Met. Mater. Trans. B 48 (2017) 889–899, https://doi.org/10.1007/s11663-016-0897-1.

[56] T. Murakami, E. Kasai, Reduction mechanism of iron oxide–carbon composite with polyethylene at lower temperature, ISIJ Int. 51 (2011) 9–13, https://doi.org/10.2355/isijinternational.51.9.

[57] P.J. Lloreda-Jurado, E.M. Pérez-Soriano, A. Paúl, J. Herguido, J.A. Peña, R. Sepúlveda, Doped iron oxide scaffolds with gradient porosity fabricated by freeze casting: pore morphology prediction and processing parameters, Mater. Sci. Technol. 36 (2020) 1227–1237, https://doi.org/10.1080/02670836.2020.1765096.

[58] S. Sen, W.F. Kaukler, P. Curreri, D.M. Stefanescu, Dynamics of solid/liquid interface shape evolution near an insoluble particle - an X-ray transmission microscopy investigation, Met. Mater. Trans. A Phys. Met. Mater. Sci. 28 (1997) 2129–2135, https://doi.org/10.1007/s11661-997-0170-y.

[59] A. Pineau, N. Kanari, I. Gaballah, Kinetics of reduction of iron oxides by H_2. Part I: low temperature reduction of hematite, Thermochim. Acta 447 (2006) 89–100, https://doi.org/10.1016/j.tca.2005.10.004.

[60] M.H. Jeong, D.H. Lee, J.W. Bae, Reduction and oxidation kinetics of different phases of iron oxides, Int. J. Hydrog. Energy 40 (2015) 2613–2620, https://doi.org/10.1016/j.ijhydene.2014.12.099.